Modeling of an electron cyclotron resonance heated mirror plasma for highly charged ion and soft x-ray sources

J. H. Booske, F. Aldabe, and R. F. Ellis
Laboratory for Plasma and Fusion Energy Studies, University of Maryland, College Park, Maryland 20742-3511

W. D. Getty
Department of Electrical Engineering and Computer Science, University of Michigan, Ann Arbor, Michigan 48109

(Received 19 November 1987; accepted for publication 24 March 1988)

A model is described for predicting equilibrium ion charge state distributions and soft x-ray emissions for highly charged ion plasmas confined in magnetic mirrors. Such a plasma would be generated and sustained with electron cyclotron resonance (ECR) heating. The model is then used to analyze a typical laboratory-sized ECR mirror plasma such as MIMI [Phys. Fluids **28**, 3116 (1985)]. Computations suggest that an experiment of this size should readily achieve a highly charged ion operating regime of relevance to studies of ECR highly charged ion plasma. In particular, these devices may be promising candidates as steady-state soft x-ray sources for x-ray lithography.

I. INTRODUCTION

Electron cyclotron resonance heated (ECRH or ECR) mirror-trapped plasmas have been demonstrated to be viable sources of highly charged ions.[1] Most recently, as discussed in Ref. 1, these high Z ions have been successfully extracted for injection into cyclotron accelerators. Other applications for such highly charged ion plasmas may include: accurate, controlled measurements of atomic processes and structures, semiconductor fabrication and materials studies, gain media for soft x-ray lasing, and incoherent soft x-ray sources (e.g., for x-ray lithography). Theoretical and experimental investigations are currently underway to evaluate the feasibility of using ECRH highly charged ion mirror plasmas for these applications.[1–7] In particular, the recent performance of such plasma as ion sources for ion cyclotrons has been very impressive. Many of the achievements, however, have been attained by designs and improvements based on simplified scaling laws, empirical "tuning," and intuitive understanding. Further improvements are likely to require better understanding of the complicated atomic and plasma physics processes—both equilibrium and dynamic—present in these plasma environments.

The purpose of the simulation study reported was threefold: (1) to extend the theoretical predictive capability for the behavior of these plasmas, (2) to evaluate the feasibility of using highly charged ion mirror plasmas for soft (incoherent) x-ray sources for x-ray lithography, and (3) to determine whether a typical laboratory-sized ECR mirror plasma experiment (specifically, the Michigan Mirror Machine "MIMI" located at the University of Michigan[8]) might achieve a highly charged ion operating regime of relevance to studies of ECR highly charged ion plasmas.

The remainder of this paper is organized in the following manner: Sec. II describes the model and computer code, while Sec. III covers typical code input parameters and the parameter space investigated for this study. Section IV is a presentation and discussion of the simulation results. In Sec. V we present a simplified model to assess the feasibility of this sort of plasma as a soft x-ray source. A summary and conclusions are presented in Sec. VI.

II. DESCRIPTION OF THE MODEL AND SIMULATION CODE

A. General model description

The simulations reported were performed with a zero-dimensional, two-part computer code entitled the electron cyclotron resonance ion and x-ray source (ECRIAXS) code. The first part (ECRIAXS-I) is a revised version of a previously developed code entitled ECRCSD[9] which calculates an equilibrium ion charge state distribution (CSD) for a given input hot electron distribution (e.g., density and average energy or "temperature"). Consequently, only a general description of the underlying physics will be presented. For further details, the reader is referred to Ref. 9 and the references contained therein. The second part (ECRIAXS-II) calculates the soft x-ray emission power spectral density (for photons between 10 and 3000 eV) and spectrally integrated emission power density (for photons between 50 and 3000 eV) for a set of equilibrium plasma conditions predicted by ECRIAXS-I.

In many theoretical calculations involving multiply charged ion species, one assumes that the equilibrium CSD results from a balance between electron impact ionization and either three-body recombination (SAHA equilibrium) or radiative recombination (coronal equilibrium).[10] For mirror-trapped ECR plasmas, however, the ion *magnetic* confinement time is often less than or equal to the radiative recombination time, and typically much less than the three-body recombination time. Thus, a proper estimate of equilibrium CSDs in ECR mirror ion sources requires a model which includes such processes as electron impact ionization, magnetic and electrostatic ion confinement, charge exchange, and recombination. ECRIAXS-I (ECRCSD) rep-

 © 1988 American Institute of Physics

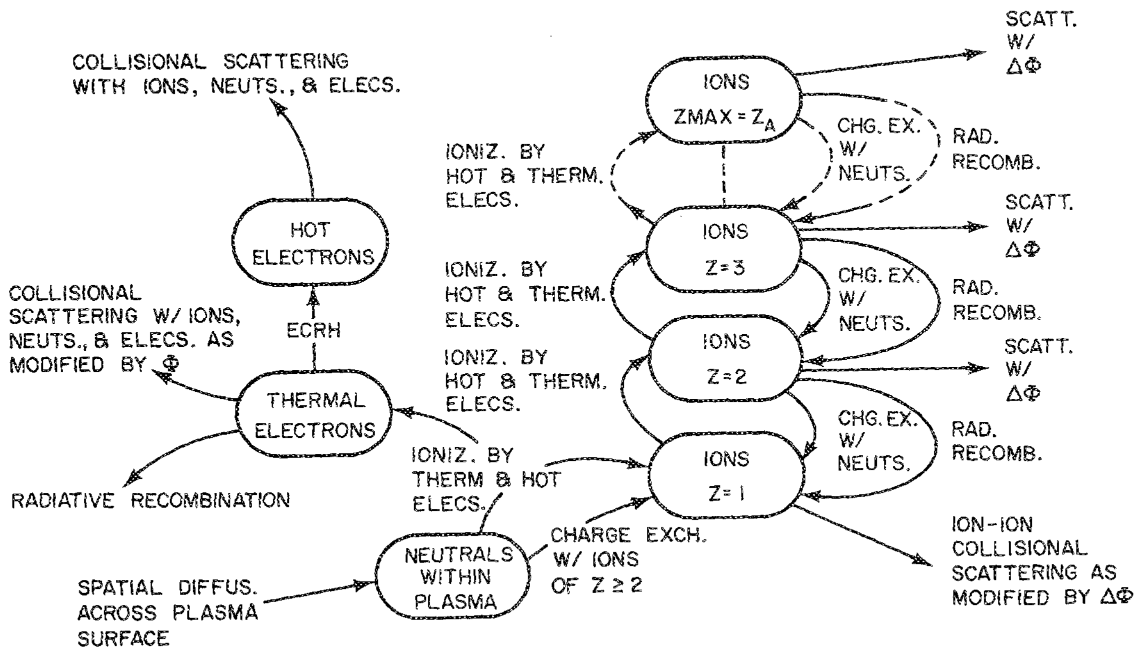

FIG. 1. Atomic and plasma transport physics in ECRIAXS.

resents an intent to incorporate these atomic and plasma processes in a single, simplified model, as indicated in Fig. 1.

Generally, the most difficult processes to model are the ion, electron, and neutral confinement processes, as they depend on the magnetic field, electrostatic potential, and plasma density spatial profiles. For the work presented, it was assumed that the ion and electron confinement were dominated by losses along the axis (i.e., parallel to magnetic flux lines). The neutral density transport, on the other hand, was assumed to be predominantly radial, consistent with an assumption that the plasma length was much greater than its characteristic radius. To quantitatively model these processes, the plasma configuration of Fig. 2 was assumed. Magnetic plasma confinement is achieved with an MHD-stable (minimum-B) magnetic mirror. Such confinement determines both the length L and the characteristic cross section of the plasma. For the cases investigated in this study, plasma cross-section shapes appropriate for several different multipole, minimum-B configurations were considered. Generally, this was only relevant for the neutral transport, and the results were relatively insensitive to the choice of cross section, provided they all had approximately the same "characteristic radius."

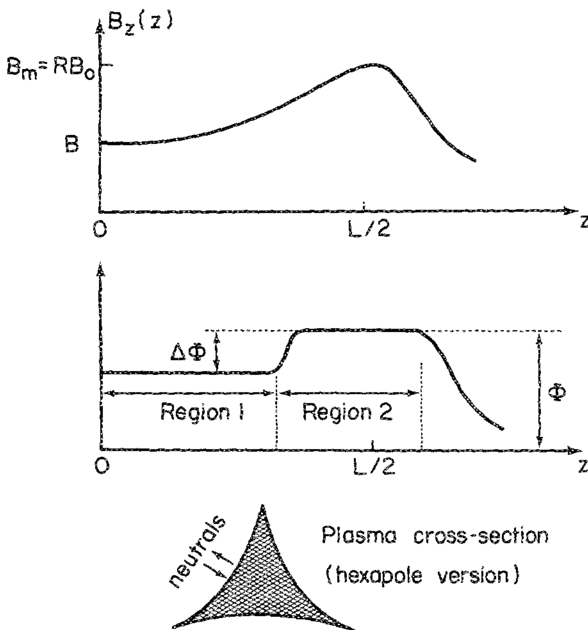

FIG. 2. Assumed plasma configuration for ECRIAXS.

The ambipolar potential profile plays an important role in the confinement of ions and electrons. For this study, the simplified "square-well" profile shown in Fig. 2 was considered representative. The potential ϕ is generally large (typically 20–100 V) and positive within the mirror region. In addition, a small potential well $\Delta\phi$ (typically 0–20 V) is maintained near the mirror midplane by a well-confined ECRH "hot" electron population. The confinement of low-energy "thermal" electrons is heavily dependent on the value of the potential peak ϕ, whereas ion containment is a sensitive function of the potential dip $\Delta\phi$.

At this point we refer back to Fig. 1 for a brief overview of the steps leading to establishment of the equilibrium plasma. The actual individual processes are nonlinearly coupled, but a qualitative understanding is possible with the following simplified model. Neutral atoms entering the plasma volume become ionized by electron impact. An ion CSD is established via a balance between further charge stripping by hot electrons and the collision-induced ion losses which depend on magnetic confinement as modified by the midplane dip in the ambipolar potential ($\Delta\phi$). The confined ions generate a positive ambipolar potential peak (ϕ) which confines sufficient thermal electrons to ensure charge quasineutrality.

Having established a model for the plasma configuration, the code aims to predict the equilibrium CSD resulting from stepwise stripping of ions from neutral to highly charged states by the energetic "hot" electrons. To accomplish this, several other important assumptions were made to facilitate the identification of mathematical formulas for the germane atomic processes. First, it was assumed that ionization is a single-step process and that the time between ionizations for a given ion is much longer than the time for the deexcitation of excited levels. The electron distribution was assumed to be comprised of two components: an energetic "hot" population (characterized by an average energy or "temperature" of $T_e^h \approx 1\text{--}10$ keV) resulting from the ECRH and a thermalized cold component (characterized by a temperature $T_e^c \approx 10\text{--}20$ eV). Such two-component modeling of ECRH electron mirror distributions is quite common and supported by many experimental studies (e.g., see Ref. 8 and the references contained therein). The ions were assumed to be thermalized at their energy of formation of a few eV. This assumption is justified by the fact that for typical ECR mirror plasmas, the ion-electron relaxation times are long compared to confinement times.

B. Solving for the equilibrium CSD in ECRIAXS-I

For neutral atom density, it is assumed that equilibrium consists of a balance between the radial flux of neutrals into the plasma volume and the burnup of neutrals within the plasma via electron impact ionization and charge exchange with ions having a charge of two or greater. Denoting the neutral densities interior and exterior to the plasma as n_{npl} and n_{no}, respectively, this balance condition can be written as

$$n_{npl} = \frac{v_{th} S/2V}{(v_{th} S/2V) + \nu_{bu}} n_{no}, \tag{1}$$

where v_{th} is the neutral thermal velocity, ν_{bu} is the neutral burnup rate, V is the plasma volume, and S is the plasma surface area. For the cases considered in this study, characteristic mean-free-path lengths for neutral-particle collisions were larger than typical radial vacuum chamber dimensions. Hence, it was assumed that the neutral temperature was in equilibrium with the chamber walls, rather than the warmer plasma ions.

Calculation of the ion CSD was based on steady-state solutions to the ion rate equations (for charge states $Z_i \geqslant 2$)

$$\begin{aligned}\frac{dn_i}{dt} &= 0\\ &\approx \nu^h_{\text{ion}_{(i-1)\to i}} n_{i-1} + \nu^{th}_{\text{ion}_{(i-1)\to i}} n_{i-1} + \nu_{cx_{(i+1)\to i}} n_{i+1}\\ &\quad + \nu_{rr_{(i+1)\to i}} n_{i+1} - (\nu^h_{\text{ion}_{i\to(i+1)}} + \nu^{th}_{\text{ion}_{i\to(i+1)}}\\ &\quad + \nu_{cx_{i\to(i-1)}} + \nu_{rr_{i\to(i-1)}} + 1/\tau_i) n_i;\\ i &= 2,3,\ldots,i_{\max}.\end{aligned} \tag{2}$$

Here, ν^h_{ion} and ν^{th}_{ion} are the hot and thermal electron impact ionization rates, respectively (multistep ionization processes are not considered), ν_{cx} is the rate of charge exchange between ions and neutrals (again, only single-step processes are considered), ν_{rr} is the rate of radiative recombination, and τ_i is the ion confinement time for midplane ions. These coupled equations can be solved recursively[9] in terms of the density of singly ionized ions. We formally write these solutions as

$$\begin{aligned} n_i &= f_i\{n_1, n_e^h, n_e^{th}, T_e^h, T_e^{th}, T_{\text{ion}}, n_{npl},\\ &\qquad \times [Z_j, C_j, \tau_j(n_1, n_2, \ldots, n_{i_{\max}}, \Delta\phi)]\};\\ j &= 2,3,\ldots,i,\end{aligned} \tag{3}$$

where C_j represents the atomic structure parameters (binding energies, etc.). By invoking quasineutrality and using f_i defined in Eq. (3),

$$\sum_{i=1}^{i_{\max}} n_i Z_i = n_1 + \sum_{i=2}^{i_{\max}} Z_i f_i = n_e^{th} + n_e^h, \tag{4}$$

one can perform an inversion described in Ref. 9 to obtain a separate equation for the midplane density of $Z=1$ ions n_1, which we formally write as

$$\begin{aligned} n_1 &= f_1\{n_e^h, n_e^{th}, T_e^h, T_e^{th}, T_{\text{ion}}, n_{n_{pl}},\\ &\qquad \times [Z_i, C_i, \tau_i(n_1, \ldots, n_{i_{\max}}, \Delta\phi)]\};\\ i &= 1,2,\ldots,i_{\max}.\end{aligned} \tag{5}$$

The model for ion confinement time is based on the suggestions of Refs. 11 and 12, generalized for charge states higher than one. Thus,

$$\tau_i \approx \tau_f(T_{\text{ion}}, \Delta\phi) + \tau_s(T_{\text{ion}}, \Delta\phi), \tag{6a}$$

$$\tau_f(T_{\text{ion}}, \Delta\phi) = RL\left(\frac{\pi m_{\text{ion}}}{2T_{\text{ion}}}\right)^{1/2} \exp\left(\frac{\Delta\phi Z_i}{T_{\text{ion}}}\right), \tag{6b}$$

$$\tau_s(T_{\text{ion}}, \Delta\phi) = \frac{\sqrt{\pi}}{2}\frac{R+1}{R}\ln(2R+2)\tau_0 P_i(\Delta\phi), \tag{6c}$$

$$P_i(\Delta\phi) = \begin{cases} \dfrac{\Delta\phi Z_i}{T_{\text{ion}}}\exp\left(\dfrac{\Delta\phi Z_i}{T_{\text{ion}}}\right), & \dfrac{\Delta\phi Z_i}{T_{\text{ion}}} > 1\\ 1, & \dfrac{\Delta\phi Z_i}{T_{\text{ion}}} \leqslant 1,\end{cases} \tag{6d}$$

where R is the mirror ratio ($R \equiv B_{\text{peak}}/B_{\text{midplane}}$), τ_f is a collisional flow time, τ_s is the mirror confinement time due to scattering and adjusted for electrostatic confinement by the potential well $\Delta\phi$,[13] and τ_0 is the classical 90° scattering time according to Spitzer.[14]

The general algorithm behind solving for steady-state CSD involves the following four steps:

(a) Assign trial values for n_i, n_e^{th}, n_e^h, T_e^h, T_e^{th}, T_{ion}, and $\Delta\phi$;

(b) Calculate a new value of n_1 using Eq. (5);

(c) Use the new value of n_1 and Eq. (3) to calculate new values for ($n_i; i \geqslant 2$); and

(d) Iterate until convergence is achieved.

In practice, however, several more calculations are performed between steps (c) and (d) to improve the accuracy and self-consistency of the model. For example, an alternative equation for the density of $Z=1$ ions n_1 which is independent of Eq. (5) can be derived by considering the equilibrium solution to the rate

equation

$$\frac{dn_1}{dt}=0$$
$$=\nu^{h}_{\text{ion}_{0\to1}}n_{npl}+\nu^{\text{th}}_{\text{ion}_{0\to1}}n_{npl}+\nu_{\text{cx}}(n_2)_{2\to1}n_{npl}$$
$$+n_{npl}\sum_{i=2}^{i_{\max}}\nu_{\text{cx}}(n_i)_{i\to(i-1)}$$
$$-(\nu^{h}_{\text{ion}_{1\to2}}+\nu^{\text{th}}_{\text{ion}_{1\to2}}+1/\tau_1)n_1. \quad (7)$$

The difference between Eq. (7) and Eq. (2) is a consequence of the fact that charge exchange between singly ionized ions and neutrals does not change the value of n_1. In contrast, every (single-step) charge-exchange reaction between a multiply ionized ion ($Z_i \geqslant 2$) and a neutral atom generates a new singly ionized ion. Furthermore, for these low charge states, radiative recombination is negligible. The solution to Eq. (7) can be written as

$$n_1=\frac{(\nu^{h}_{\text{ion}_{0\to1}}+\nu^{\text{th}}_{\text{ion}_{0\to1}}+\nu_{\text{cx}_{2\to1}}+\sum_{i=2}^{i_{\max}}\nu_{\text{cx}_{i\to(i-1)}})n_{npl}}{\nu^{h}_{\text{ion}_{1\to2}}+\nu^{\text{th}}_{\text{ion}_{1\to2}}+1/\tau_1}. \quad (8)$$

Solutions (5) and (8) for n_1 can be equated and solved for n_e^{th}.[9] We formally write this solution as

$$n_e^{\text{th}}=F\{n_e^h,T_e^h,T_e^{\text{th}},T_{\text{ion}},n_{npl},[Z_i,C_i,\tau_i(n_1,\ldots,n_{i_{\max}})],\ \Delta\phi\};$$
$$i=1,2,\ldots,i_{\max}. \quad (9)$$

Note that Eq. (9) represents a relation between n_e^{th} and $\Delta\phi$. An alternative, independent relationship between n_e^{th} and $\Delta\phi$ can be obtained, however, by generalizing a model in Ref. 12 for multiply charged ions. First, it is assumed that the hot electrons are well trapped near the mirror midplane so that closer to the mirror throat (region 2 in Fig. 2). There are few hot electrons, and consequently

$$n_{e,m}=n^{\text{th}}_{e,m}+n^{h}_{e,m}\simeq n^{\text{th}}_{e,m}.$$

Here, the additional "m" subscript refers to mirror throat quantities, as distinct from mirror midplane (region 1 in Fig. 2) quantities. Second, it is assumed that quasineutrality exists near the mirror throat so that

$$n^{\text{th}}_{e,m}\simeq\sum_{i=1}^{i_{\max}}n_{i,m}Z_i.$$

Third, it is assumed that the thermal electrons are Boltzmann distributed between regions 1 and 2:

$$n^{\text{th}}_{e,m}\simeq n_e^{\text{th}}\exp(\Delta\phi T_e^{\text{th}}).$$

Finally, axial fluxes of ions and electrons out of both regions 1 and 2 are balanced so as to ensure steady-state ambipolar potentials. This results in the approximate relation[9,12]

$$n^{\text{th}}_{e,m}\simeq\tau_f\sum_i\frac{n_iZ_i}{\tau_i}$$

or

$$n_e^{\text{th}}\simeq\exp\left(\frac{-\Delta\phi}{T_e^{\text{th}}}\right)\tau_f\sum_i\frac{n_iZ_i}{\tau_i(\Delta\phi)}. \quad (10)$$

Equations (9) and (10) can now be solved simultaneously by the Newton–Raphson method to obtain self-consistent (within the limits of the models) solutions of n_e^{th} and $\Delta\phi$.

A solution can also be obtained for the peak potential ϕ which is self-consistent with the thermal electron density by invoking a balance of ambipolar endloss currents:

$$\frac{n_e^h}{\tau_e^h}+\frac{n_e^{\text{th}}}{\tau_e^{\text{th}}}=\sum_i\frac{n_iZ_i}{\tau_i}, \quad (11a)$$

where

$$\tau_e^{\text{th}}\equiv\tau_f(T_e^{\text{th}},\phi)+\tau_s(T_e^{\text{th}},\phi), \quad (11b)$$

and τ_f and τ_s have been previously defined in terms of ion parameters and $\Delta\phi$ [cf. Eqs. (6)]. Equations (11) can be rearranged to solve for self-consistent values of ϕ via the Newton–Raphson method, as described in Ref. 9.

In summary, Eqs. (1), (3), (5), and (9)–(11) are solved iteratively for equilibrium values of n_i, n_e^{th}, ϕ, $\Delta\phi$, and n_{npl}, which are self-consistent within the model approximations. Although this appears to be a monumental numerical task, for the cases considered for this study it was usually possible to determine the existence of an equilibrium and the equilibrium solutions within 10 to 50 iterations.

C. Theoretical models for atomic processes in ECRIAXS-I

The dominant atomic processes required for the model described above include ionization, ion-neutral charge exchange, and radiative recombination. Charge-exchange rates were computed from the cross-section model of Ref. 15, averaged over a Maxwellian ion distribution. From the formula for dielectronic recombination found in Ref. 16 it can be determined that for the plasma conditions considered in this study (e.g., $T_e^h \geqslant 1000$ eV, $T_e^{\text{th}}\simeq 10$ eV, $n_{npl}\sim 10^{11}$ cm^{-3}, $n_i\sim 10^{11}$–10^{12} cm^{-3}, and $Z_i<20$) dielectronic recombination is much less than charge exchange for all relevant ion states.

The ionization rates in ECRIAXS-I were calculated using the model of Lotz.[17] This formula includes inner—as well as outer—shell ionization processes. The ionization rate calculations were supplemented by the ionization potential and subshell binding energy formulas of Carlson *et al.*[18] Finally, radiative recombination was calculated by the model used in Ref. 19.

D. Model limitations in ECRIAXS-I

In order to obtain an understanding of some of the basic physics of ECR ion and x-ray sources and yet avoid excessive numerical complexity, we have attempted to use the simplest model that is still relevant to the physical system of interest. In so doing, we have ignored some effects that may be important in actual experimental devices. It is intended that future advanced studies will incorporate some of these effects into the modeling so as to ascertain their relative importance. It has been suggested[2,20] that for the very highly charged ions (e.g., $Z_i \gtrsim 10$–15 in argon) ion-ion collision rates become so high that the ion confinement time represented by Eqs. (6) is more accurately described by an axial spatial diffusion time. While ECRIAXS-I does include inner shell ionization via the Lotz formula,[16] it ignores the possibilities of inner shell excitation (i.e., excitation not resulting in ionization) and/or metastable excited state formation (see, for example, Ref.

21 and references contained therein). Electron confinement time models in ECRIAXS-I do not consider the effects of rf-enhanced diffusion.[22] Possibilities for increased particle end-losses due to microinstabilities are ignored. In addition, resonant radial ion transport due to the nonaxisymmetric minimum-B fields is not considered.

E. Theoretical models used in ECRIAXS-II

The bulk of the computations in ECRIAXS-II involve calculating model x-ray emission power spectral densities (i.e., power emitted per unit volume per unit photon frequency or energy). In particular, ECRIAXS-II computes these spectral densities as if they were measured with a spectrally resolving diagnostic having a minimum spectral resolution of 3 eV:

$$\frac{dW}{dV}(E_j) \approx \frac{1}{\Delta E}\int_{E_j-(\Delta E/2)}^{E_j+(\Delta E/2)} dE\, \frac{dW}{dV}(E)\,\mathrm{W/(cm^3\ eV)}. \tag{12}$$

Here, $dW/dV(E_j)$ represents the "discreetly sampled" x-ray power spectral density as defined above and $\Delta E \approx 3$ eV. ECRIAXS-II also computes the spectrally integrated power density between 50 and 3000 eV (a band of interest to x-ray photolithography):

$$\frac{dP_{\mathrm{total}}}{dV} = \int_{50\,\mathrm{eV}}^{3000\,\mathrm{eV}} dE\left(\frac{dW_{\mathrm{ff}}}{dV} + \frac{dW_{\mathrm{bf}}}{dV} + \frac{dW_{\mathrm{bb}}}{dV}\right)\ \mathrm{W/cm^3}. \tag{13}$$

The subscripts "ff," "bf," and "bb" refer to free-free (bremsstrahlung), free-bound (recombination), and bound-bound (line) radiation, respectively.

To compute the bremsstrahlung emission we model the plasma with hydrogen like ions to obtain[23]

$$\frac{dW_{\mathrm{ff}}}{dV}(E) \approx \kappa_1 \sum_{k=h,\mathrm{th}} \sum_{i=1}^{Z_A} n_e^k n_i Z_i^2 \left(\frac{\chi_{\mathrm{H}}}{T_e^k}\right)^{1/2} \exp\left(\frac{-E}{T_e^k}\right)$$
$$\mathrm{W/(cm^2\ eV)}, \tag{14}$$

where $\kappa_1 \approx 7.17\times10^{-33}$ (W cm^3)/eV, n_e and n_i are the electron and ion densities in cm^{-3}, Z_A is the atomic number of the element, χ_{H} is the hydrogen ionization potential, and all energy quantities (e.g., χ_{H}, E, and T_e) are in eV. We note that rigorously, Eq. (14) lacks generality due to the omission of Gaunt factors (i.e., we have assumed that $g_{\mathrm{ff}} \approx 1$, for all cases). An extensive discussion of the Gaunt factors for hydrogenic ions is presented in Ref. 24, while a more abbreviated description can be found in Ref. 25. A careful study of Fig. 1.3.4 on p. 91 of Ref. 25 reveals, however, that the Gaunt factors only have significant deviations from 1.0 when $Z_i^2\chi_{\mathrm{H}}/T_e$ and $E/(Z_i^2\chi_{\mathrm{H}})$ are both less than 1.0. Hence Eq. (14) is only in error for low Z_i, high T_e, and low photon energy E. In the particular case where $E \approx 50$ eV and $T_e \approx 3$ keV, g_{ff} (the free-free Gaunt factor) only deviates significantly from 1.0 for $Z_i \approx 3$–5. Even in this case, there are several mitigating factors. First, for 50-eV photons, the bremsstrahlung emission at $T_e \approx 3$ keV is significantly reduced below its peak value (at $T_e \approx 100$ eV) due to the $T_e^{-1/2}$ scaling. Second, as we shall see later, for the parameter regimes investigated in this study the bremsstrahlung emission is usually insignificant compared to line emission in the 50- to 3000-eV photon energy band. Nevertheless, future applications of the model over larger parameter ranges will require addition of these Gaunt factor corrections to the bremsstrahlung emission.

From Refs. 23 and 26 one can estimate the x-ray power spectral density from all free-bound electron transitions (in hydrogen-like ions) as

$$\frac{dW_{\mathrm{bf}}}{dV}(E) \approx \kappa_1 \sum_{k=h,\mathrm{th}} \sum_{i=1}^{Z_A} \sum_{m=m_{\min}}^{\infty} n_e^k n_i \left(\frac{\chi_{\mathrm{H}}}{T_e^k}\right)^{3/2}$$
$$\times\left(\frac{\chi_i}{\chi_{\mathrm{H}}}\right)^2 \frac{g_{\mathrm{bf}}}{m^3} \exp\left(\frac{(\chi_i/m^2) - E}{T_e^K}\right)$$
$$\mathrm{W/(cm^2\ eV)}, \tag{15}$$

where χ_i is the ground state ionization potential to elevate a Z_{i-1} ion to the Z_i charge state, m is the excited state quantum index (hydrogenic model), and $m_{\min}$ is the smallest positive integer satisfying

$$m_{\min} \geqslant (\chi_i/E)^{1/2}.$$

Estimating the x-ray emission from bound-bound transitions is a more complicated effort and generally requires modeling approximations. The model described here was based on equations and suggestions taken from Refs. 23 and 26. Basically, it assumes that within a specific charge state there exists a coronal equilibrium between collisional excitation due to electron-ion collisions and spontaneous radiative decay. First, the x-ray power density emitted by ith-type ions (with charge state Z_i) undergoing bound electron decay transitions from the E_p (upper) to the E_q (lower) energy level can be written as

$$\frac{dP_{\mathrm{bb}}}{dV}(i,p\to q) \approx n_e^h n_i(1) X(T_e^h,E_1,E_p)$$
$$\times\left(A(p,q)\Big/\sum_{q<p} A(p,q)\right)\chi(p,q). \tag{16}$$

Here, n_e^h is the hot electron density, $n_i(1)$ is the density of those i-type ions which populate the ground ($p=1$) state, $X(T_e,E_1,E_p)$ is the collisional excitation rate coefficient for ground state (E_1) i-type ions undergoing transition to the upper excited state (E_p) due to collisions with electrons having temperature T_e, $A(p,q)$ is the transition probability for the radiation transition from E_p to E_q and $\chi(p,q)$ is the energy difference, $\chi(p,q) \equiv E_p - E_q$. For n_e^h and $n_i(1)$ in cm^{-3}, $X(T_e^h,E_1,E_p)$ in cm^3/s, and $\chi(p,q)$ in J, dP_{bb}/dV is in W/cm^3. From Ref. 10, $X(T_e,1,p)$ can be estimated as

$$X(T_e 1,p) \approx \frac{(8.5\times10^{-4})\bar{g}f(p,1)}{(T_e)^{1/2}\chi_e(p,1)}$$
$$\times\exp\{-[(1.16\times10^4)\chi_e(p,1)]/T_e\}, \tag{17}$$

where $f(p,1)$ is the oscillator line strength for the ground-to-p-level transition, $\chi_e(p,1)$ is the excitation energy of the p level (relative to the ground state) in eV, $\bar{g}$ is an "averaged" Gaunt factor, and T_e and $X(T_e,1,p)$ are in K and cm^3/s, respectively. The above formula was obtained by performing a Maxwellian average (over electron velocities) of the electron impact excitation cross section due to Seaton.[27]

The first approximation made is to assume that of all the possible radiative decay transitions from the p level to any lower q level, the p-to-ground ($p \to 1$) transition dominates. Symbolically, this is expressed as

$$A(p,1) \Big/ \sum_{q=1}^{p-1} A(p,q) \sim 1.$$

Hence,

$$\begin{aligned} \sum_q \frac{dP_{\rm bb}}{dV}(i,p\to q) &\approx \frac{dP_{\rm bb}}{dV}(i,p\to 1) \\ &\approx n_e^h n_i(1)\{[(1.4\times 10^{-22})\bar{g}f(p,1)]/(T_e^h)^{1/2} \\ &\quad \times \exp\{-[(1.16\times 10^4)\chi_e(p,1)]/T_e^h\}\}. \end{aligned} \tag{18}$$

In Eq. (18), the power density is in W/cm^3 if n_e^h and $n_i(1)$ are in cm^{-3}, T_e^h is in K, and $\chi_e(p,1)$ is in eV units. The next important assumption is to assume that most of the radiation from (excited) i-type ions will come from the resonance line (i.e., $E_p \to E_1 \approx E_2 \to E_1$). Symbolically,

$$\begin{aligned} \sum_p \sum_q \frac{dP_{\rm bb}}{dV}(i,p\to q) &\approx \sum_p \frac{dP_{\rm bb}}{dV}(i,p\to 1) \\ &\approx \frac{dP_{\rm bb}}{dV}(i,2\to 1). \end{aligned}$$

For quantitative purposes, Griem[26] recommends

$$\begin{aligned} \frac{dP_{\rm bb}}{dV}(i) &\approx \sum_p \frac{dP_{\rm bb}}{dV}(i,p\to 1) \\ &\approx n_e^h \frac{(1.4\times 10^{-22})\bar{g}}{(T_e^h)^{1/2}} \\ &\quad \times \sum_p n_i(1) f(p,1) \exp\left(-\frac{(1.16\times 10^4(\chi_e(p,1))}{T_e^h}\right) \\ &\approx n_e^h \frac{(1.3\times 10^{-24})}{[T_e^h(\text{eV})]^{1/2}} [(0.5)n_i] \exp\left(\frac{-\chi_e(2,1)}{T_e^h(\text{eV})}\right), \end{aligned} \tag{19}$$

where in Eq. (19), $n_i \equiv \Sigma_p n_i(p)$ is the total density of all ith charge-state ions (in cm^{-3}), χ_e (2,1) is the energy of the resonance transition (in eV), n_e^h is the hot electron density (in cm^{-3}), and $(dP_{\rm bb}/dV)(i)$ is in W/cm^3. To quantitatively specifiy $\chi_e(2,1)$, we consider the hydrogen like atomic (Bohr) model for bound electron energy levels:

$$E_p \approx E_1/p^2, \quad p = 1,2,3,\ldots,\infty, \tag{20}$$

where E_1 is the ground state energy and p is the principal quantum number. From Eq. (20) it is clear that the energy of the resonance transition for hydrogen-like ions is approximately

$$\chi_e(2,1) = |E_2 - E_1| \approx (0.75)E_1. \tag{21}$$

Strictly speaking, a self-consistent calculation based on the Bohr model would use

$$E_1(i) \approx Z_i^2 \chi_{\rm H}, \tag{22}$$

where $E_1(i)$ is the ground state ionization potential for the outermost electron of Z_i charge-state ions and $\chi_{\rm H} \approx 13.6$ eV is the ionization potential for monatomic hydrogen (also known as Rydberg's constant). For our calculations, however, we chose a "hybrid" resonance line model based on Eq. (21) but using tabulated values for E_1 [e.g., see Ref. 28 instead of Eq. (22)]. To convert the power density into a power spectral density, we incorporate a Dirac delta function notation, consistent with the dominant resonance line assumption. Finally, it has been recommended[26] to use $\bar{g} \approx 0.2$ for the averaged Gaunt factor. The result of all these considerations is

$$\frac{dW_{\rm bb}}{dV}(E) \approx \sum_{i=1}^{Z_A} \kappa_2 n_e^h n_i (T_e^h)^{1/2} \exp\left(-\frac{E}{T_e^h}\right) \delta(E - \chi_i^{\rm res}) \quad \text{W/cm}^3\,\text{eV}, \tag{23}$$

where $\kappa_2 = 1.3\times 10^{-25}$, $\chi_i^{\rm res} \equiv E_{2,i} - E_{1,i} \approx (0.75)E_{1,i}$, n_e^h and n_i are in cm^{-3}, T_e^h and $E_{1,i}$ are in eV, and Z_A is the atomic number of the element.

F. Model limitations in ECRIAXS-II

As in ECRIAXS-I, the radiation section of our model has omitted several processes. Specifically, we mention two of those processes, along with estimates of their probable impact on the model predictions. First, it has been found that for nonhydrogenic ions (i.e., ions with two or more electrons in the outer shell) in "low-density" plasmas (i.e., $n_e \leqslant 10^{16}$ cm^{-3}) the hydrogenic model for bound-bound radiation is incomplete.[19,25] Specifically, for such cases, bound-bound transitions in which the outer most electron does not change principal quantum number [viz., "p" in Eq. (20)] may be important. These transitions are currently not included within our model. In addition, for the indicated $\Delta p = 0$ transitions, use of a Gaunt factor $\bar{g} \approx 0.2$ is also inaccurate. Based on the results cited in Refs. 19 and 25, it is estimated that inclusion of these transitions would enhance integrated radiation power levels by a factor of approximately two, while using more accurate Gaunt factors would roughly introduce an additional increase of two.[29] Furthermore, the bulk of this radiation component would tend to occur at photon energies below 100 eV for lower Z_A atomic species (i.e., $Z_A \leqslant 10$), whereas for higher Z_A materials (i.e., $Z_A \geqslant 18$) the emission would be concentrated in the 50–150 eV band.[19]

A second feature not currently included in ECRIAXS-II involves inner shell processes. While ECRIAXS-I includes a model for inner shell ionization, our radiation model does not include fluorescent yields resulting from the inner-shell vacancies (see, for example, Ref. 30). Consequently, the computations presented may underestimate radiation power levels at the higher photon energies $E \sim T_e^h$.

It is planned that for future studies, revisions will be incorporated in our model to correct some of the omissions cited above. For the present work, however, it has been estimated that inclusion of the two line radiation processes described above would yield a factor of 2–5 increase in the total integrated power. The effects of the x-ray spectra, however, would tend to be offsetting in such a manner that the basic profiles would remain similar to those predicted here (albeit,

with considerably more detail).[29] Hence, for the purposes of evaluating the feasibility of ECRIS plasmas for soft x-ray lithography applications, the results presented in this article are considered to be reasonably accurate with any errors being on the conservative side.

III. TYPICAL CODE INPUTS AND OUTPUTS AND PARAMETER SPACE INVESTIGATED

Code inputs describe the mirror plasma geometry, atomic data for the elemental species considered, neutral gas base pressure, anticipated final equilibrium values for some parameters relevant to plasma particle distributions, and initial guesses for those plasma parameters which ECRIAXS-I calculates self-consistently. For example, mirror plasma configuration input parameters include a characteristic plasma length, "radius," cross-sectional shape, etc. Atomic input data includes the atomic mass and number, tabulated ionization potentials, Lotz[17] coefficients, and neutral atom binding energies. Plasma particle distribution input parameters are $n_e^h, T_e^h, T_{\text{ion}}$, and T_e^{th}. The neutral base pressure is fixed by specifying an input value for n_{no}. Initial guesses for n_e^{th} and $\Delta\phi$ are also required as input.

Code outputs from ECRIAXS include the self-consistent values for the densities and potentials: $n_e^{\text{th}}, \Delta\phi, \phi$, and $\{n_i\}$ (i.e., the CSD). Also provided are estimates of the equilibrium particle and energy loss rates from the plasma, the x-ray emission spectra between 10 and 3000 eV, and the integrated total x-ray power density for photons between 50 and 3000 eV.

The parameter space investigated for this study was limited to regimes typical of "small-scale" experimental mirror devices such as MIMI.[8] In particular, we considered a (mirror-to-mirror) plasma length of 50 cm, a "characteristic plasma radius" of 2 cm, and a plasma mirror ratio $R = 2$. The atomic species considered included hydrogen, helium, nitrogen, oxygen, neon, argon, iron, and krypton for neutral base pressures (external to the plasma) of 0.5, 1.0, and 2.0×10^{-6} Torr. Hot electron distribution parameters of $n_e^h = 0.5$, 1.0×10^{12} cm^{-3} and $T_e^h = 3$, 10 keV were used. The ion temperature was fixed at a nominal 5 eV and the thermal electron temperature was chosen to be 10 eV.

IV. SIMULATION RESULTS AND DISCUSSION

The first simulation results studied were the predicted equilibrium values of the hot electron fraction, $n_e^h/(n_e^h + n_e^{\text{th}})$, versus elemental atomic number Z_A for the different neutral pressures and hot electron parameters considered. Experimental experience indicates that this fraction is closely related to both micro- and macrostability of the plasma. Consequently, the values of the theoretically predicted hot electron fractions provide a qualitative measure of one's confidence in experimentally achieving the theoretical equilibrium states. The results are presented in Fig. 3, showing that the lowest hot electron fractions are associated with the higher Z atomic species. Although there is still an incomplete physical understanding regarding what fraction of hot electrons is desirable with respect to plasma stability under various plasma conditions (cf. Refs. 8, 31, and 32, and refer-

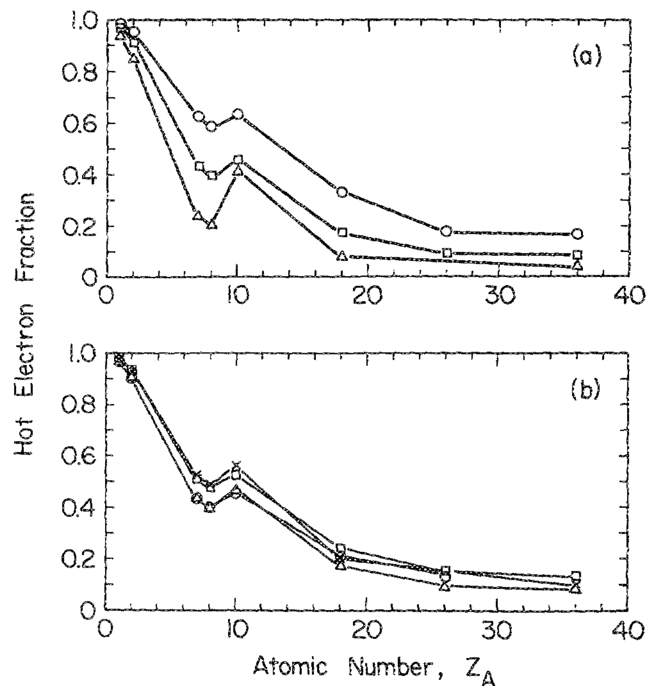

FIG. 3. Hot electron fraction $n_e^h/n_e^h + n_e^{\text{th}})$ vs atomic number Z_A (a) for different neutral pressures ($n_e^h = 5 \times 10^{11}$ cm^{-3}, $T_e^h = 3$ keV): $p_n = 0.4 \times 10^{-6}$ Torr (circles), 1.0×10^{-6} Torr (squares), 2.0×10^{-6} Torr (triangles); (b) for different hot electron parameters ($p_n = 1.0 \times 10^{-6}$ Torr): 1.0×10^{12} cm^{-3} and 3.0 keV (circles), 1.0×10^{12} cm^{-3} and 10.0 keV (squares), 5.0×10^{11} cm^{-3} and 3.0 keV (triangles), 5.0×10^{11} cm^{-3} and 10.0 keV (crosses).

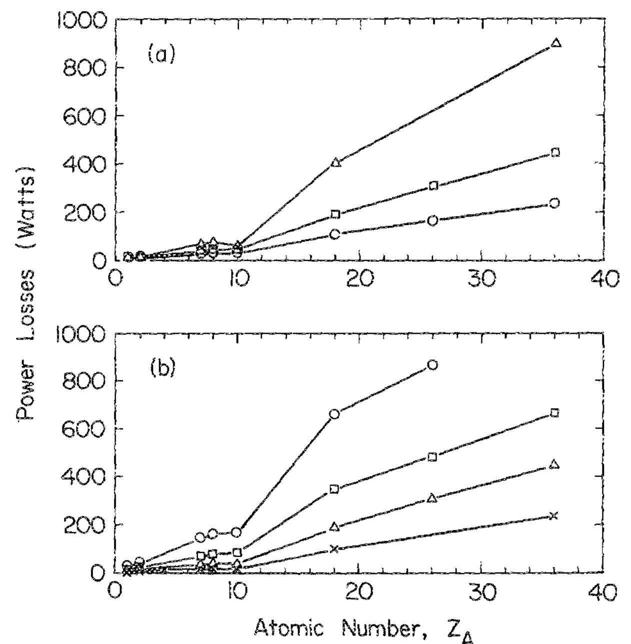

FIG. 4. Minimum ECRH power necessary to balance the equilibrium plasma energy loss rate. (a) For different neutral pressures ($n_e^h = 5 \times 10^{11}$ cm^{-3} and $T_e^h = 3$ keV): $p_n = 0.5 \times 10^{-6}$ Torr (circles), 1.0×10^{-6} Torr (squares), 2.0×10^{-6} Torr (triangles); (b) for different hot electron parameters ($p_n = 1.0 \times 10^{-6}$ Torr): 1.0×10^{12} cm^{-3} and 3.0 keV (circles), 1.0×10^{12} cm^{-3} and 10.0 keV (squares), 5.0×10^{11} cm^{-3} and 3.0 keV (triangles), 5.0×10^{11} cm^{-3} and 10.0 keV (crosses).

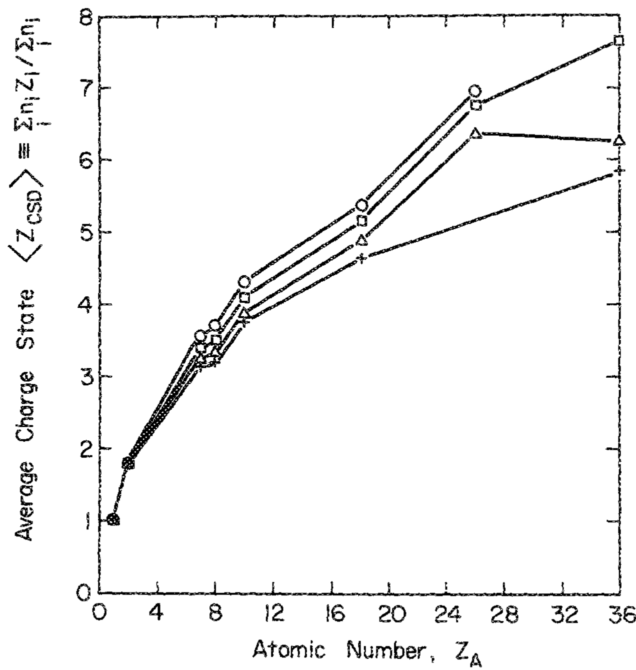

FIG. 5. Average CSD charge state vs atomic number for different hot electron parameters: 1.0×10^{12} cm^{-3} and 3.0 keV (circles), 1.0×10^{12} cm^{-3} and 10.0 keV (squares), 0.5×10^{12} cm^{-3} and 3.0 keV (triangles), 0.5×10^{12} cm^{-3} and 10.0 keV (crosses) ($p_n = 1.0\times10^{-6}$ Torr in all cases).

ences contained therein), one is more likely to believe that the high Z predictions (with lower hot electron fraction) are more achievable in experiments than the extremely high hot electron fractions associated with the lower Z plasmas. The low Z cases, for example, may be more susceptible to (micro) instability-enhanced transport in an actual experiment and this transport mechanism is not included in the simulation model.

Another feature impacting our confidence in the relevance of the simulations to experimental devices was the minimum ECRH power levels necessary to sustain the predicted equilibria. If we assume that the ECRH power levels must balance particle and radiative energy loss rates, then we can see from Fig. 4 that the absorbed ECRH power must typically be on the order of 100–1000 W. Such power levels are easily achievable with modern cw microwave tubes—even with allowances for incomplete power absorption.

In Fig. 5, we have plotted the predicted average charge state of the CSD, $\langle Z_{CSD}\rangle$, versus the atomic number of the element used for the plasma. The increase in highly charged ions gained by using heavier elements is evident. From these results it is also apparent that higher hot electron densities ($n_e^h \geqslant 1.0\times10^{12}$ cm^{-3}) but more moderate hot electron temperature ($T_e^h \approx 3$ keV) produce higher average charge states. Figure 6 is a representative example of the type of

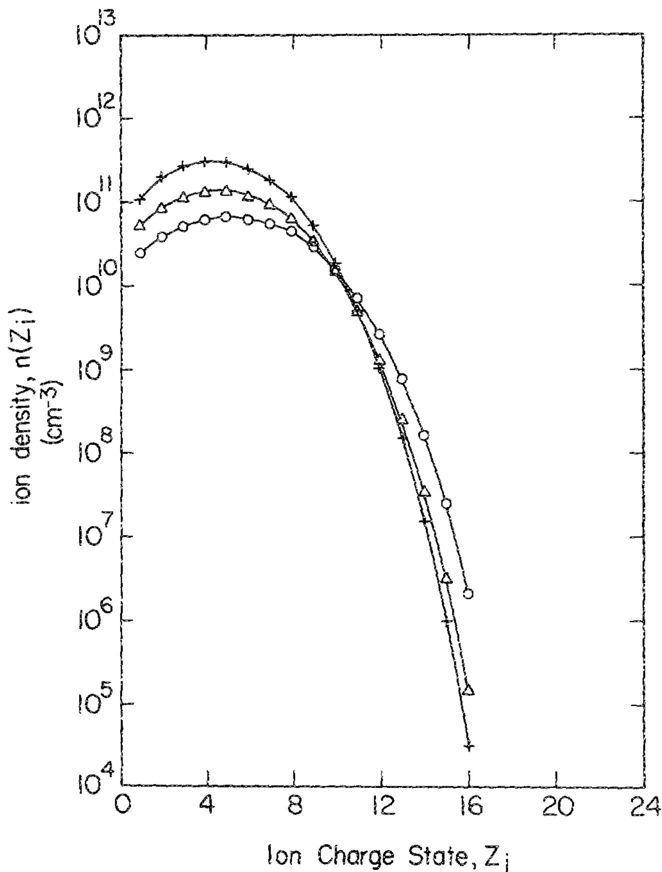

FIG. 6. Equilibrium argon ion charge state distributions predicted for a MIMI-like ECR ion source. The three curves correspond to neutral argon gas pressures of 0.5×10^{-6} Torr (circles), 1.0×10^{-6} Torr (triangles), and 2.0×10^{-6} Torr (crosses). Other parameters are $n_e^h = 10^{12}$ cm^{-3}, $T_e^h = 10$ keV, $T_e^{th} = 10$ eV, and $T_i = 5$ eV.

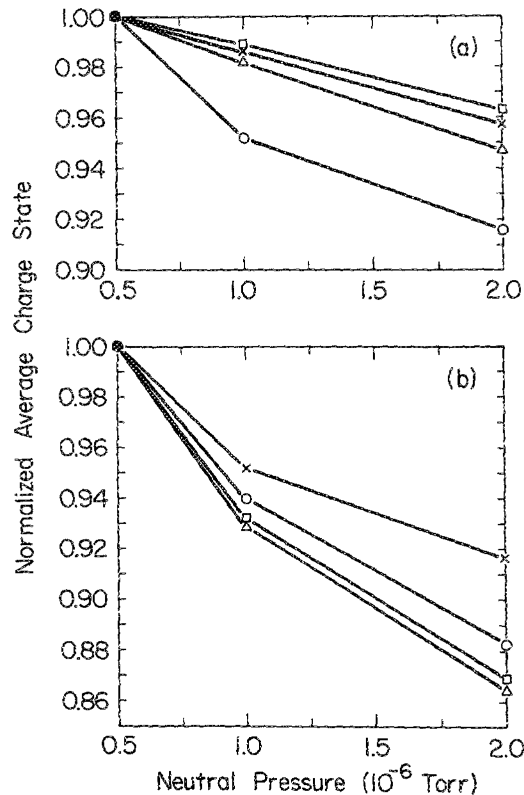

FIG. 7. Relative (normalized) dependence of the CSD average charge state $\langle Z_{CSD}\rangle$ vs neutral pressure. (a) For argon using different hot electron parameters: 1.0×10^{12} cm^{-3} and 3.0 keV (circles), 1.0×10^{12} cm^{-3} and 10.0 keV (squares), 5.0×10^{11} cm^{-3} and 3.0 keV (triangles), 5.0×10^{11} cm^{-3} and 10.0 keV (crosses); (b) for different atomic species: nitrogen (circles), oxygen (squares), neon (triangles), and argon (crosses), with hot electron parameters of 1.0×10^{12} cm^{-3} and 3.0 keV.

equilibrium CSDs one might achieve with a device such as MIMI and an argon plasma. The difference between the three cases shown is a result of varying the background argon pressure between 0.5×10^{-6} Torr (circles), 1.0×10^{-6} Torr (triangles), and 2.0×10^{-6} Torr (crosses). Otherwise, all relevant plasma parameters were held constant to the values indicated in the figure caption. As seen in Fig. 6, appreciable densities ($n_i \gtrsim 10^9$ cm^{-3}) of ions are predicted for charge states as high as AR XII. Note that at lower neutral base pressures, there was a tendency towards lower total ion density concurrent with an increase in the relative fraction of high Z ions. This is consistent with a combination of lower ionization rates and higher hot electron fractions [cf. Fig. 3(a)] observed at lower neutral pressures.

In Fig. 7, we have plotted the (normalized) average charge state versus neutral pressure. These results confirm that the qualitative trend towards higher average charge state with decreasing neutral pressure (shown in Fig. 6) was also true for the other plasmas investigated.

A typical x-ray emission spectrum for an argon plasma is presented in Fig. 8 where the relative contributions from bremsstrahlung, line, and recombination radiation have been separately indicated along with the composite spectrum. Perhaps the most important feature to observe is that the line radiation tends to dominate the emission spectrum, especially at the lower energies (e.g., less than approximately 500 eV). In fact, the line radiation component accounts

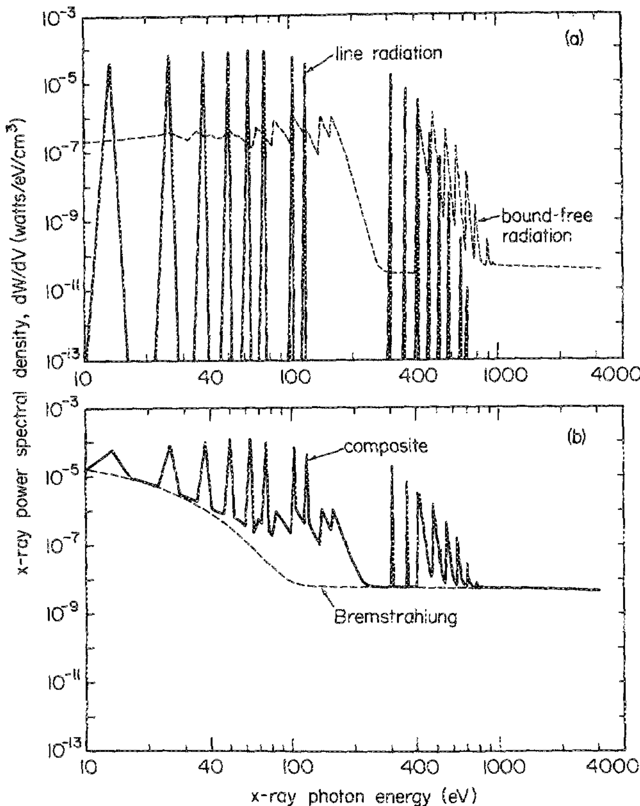

FIG. 8. Typical x-ray power spectral density for argon plasma with $p_n = 2\times10^{-6}$ Torr, $n_e^h = 1.0\times10^{12}$ cm^{-3}, and $T_e^h = 10.0$ keV. (a) Line (solid) and bound-free or recombination (dashed) spectra, and (b) bremsstrahlung (dashed) and the total composite (solid) spectra.

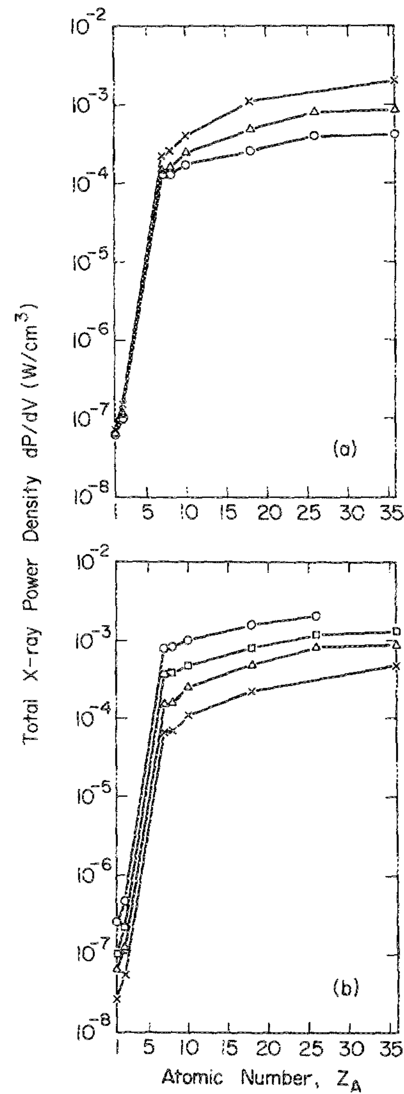

FIG. 9. Total x-ray emission power density (spectrally integrated from 50 to 3000 eV) vs atomic number. (a) For different neutral pressures ($n_e^h = 5.0\times10^{11}$ cm^{-3}, $T_e^h = 3.0$ keV): $p_n = 0.5\times10^{-6}$ Torr (circles), 1.0×10^{-6} Torr (triangles), 2.0×10^{-6} Torr (crosses); (b) for different hot electron parameters ($p_n = 1.0\times10^{-6}$ Torr): 1.0×10^{12} cm^{-3} and 3.0 keV (circles), 1.0×10^{12} cm^{-3} and 10.0 keV (squares), 5.0×10^{11} cm^{-3} and 3.0 keV (triangles), 5.0×10^{11} cm^{-3} and 10.0 keV (crosses).

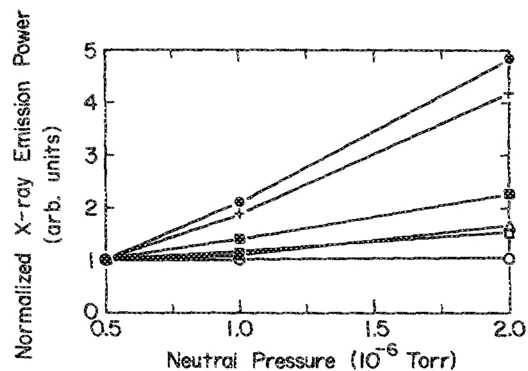

FIG. 10. Total x-ray emission power (normalized) vs neutral pressure for hydrogen (open circles), helium (open squares), nitrogen (triangles), neon (filled squares), argon (crosses), and krypton (filled circles) ($n_e^h = 5.0\times10^{11}$ cm^{-3}, $T_e^h = 3.0$ keV).

for approximately 90% of the total spectrum-integrated power density [cf. Eq. (13)] between 50 and 3000 eV for the spectrum shown in Fig. 8. This effect was generally true for all cases considered in these simulations.

The spectrally integrated (50 to 3000 eV) emission power densities as a function of atomic number have been plotted in Fig. 9. Clearly, plasmas based on elements having higher atomic number yielded higher predicted x-ray power densities. Perhaps not quite so expected are the additional predictions that higher x-ray emissions are associated with *higher* neutral pressures and higher density but less energetic hot electron distributions. In Fig. 10, we have also plotted the total x-ray emission power densities (normalized) versus neutral pressure. Once again, the enhancement of x-ray emission with increasing neutral pressure is evident. Figures 9 and 10 can be explained in the following manner. First, typical electron-ion collision frequencies increase linearly with electron density but decrease with higher electron energies above a few keV or so. Consequently, one might expect that higher hot electron densities but more modest hot electron temperatures result in higher ion densities and higher ion excitation rates. This is consistent with the results shown in Fig. 5. Also, in view of the fact that the x-ray output was principally line radiation, we can see from the exponential factor in Eq. (23) that this component of emission is dominated by x-rays coming from transitions in the lowest charge state ions (e.g., $Z_i \lesssim 5$). In Figs. 6 and 7, however, it was observed that higher absolute densities for these lower charge states were associated with higher neutral base pressures. These facts combine to produce the trends seen in Figs. 9 and 10.

A note of caution should be mentioned regarding the higher x-ray power levels at lower hot electron temperatures. This observation may be influenced by the omission in ECRIAXS-II of fluorescent line radiation associated with inner shell ionization. Higher hot electron energies, for example, permit greater atomic shell penetration possibly resulting in increased line radiation for increasing T_e^h (in spite of reduced collision frequencies). This behavior is a subject for future study.

V. SOFT X-RAY SOURCE FEASIBILITY ASSESSMENT

Numerous features must be evaluated on a comparative basis when proposing a soft x-ray source for photolithography. First, it is preferable to have the x-ray photon energies within the most sensitive photoresist exposure bands (e.g., approximately 50 to 3000 eV). Of course, it is desirable to have a large output x-ray flux, although the requirements on x-ray intensity for a continuously radiating source may be somewhat less than for a pulsed device, as average power is more relevant to wafer exposure time. It may also be important to consider the impact of an expensive and/or sophisticated source technology versus a more modest-priced, simpler source technology. For example, in a comparison of synchrotron, pulsed plasma (either discharge or laser ablation), and ECR mirror plasma sources, the synchrotron may be expensive and require more sophisticated operating techniques, whereas pulsed plasma sources may require increased maintenance due to electrode (or target) erosion and/or other stresses associated with repetitively pulsed high-power systems. ECR mirror plasmas, on the other hand, may be able to provide an alternative source of soft x-ray using well established and relatively unsophisticated magnet and microwave source technologies. Of course, this would not preclude the use of more exotic (and perhaps more expensive) superconducting magnet and high-power gyrotron technologies for ECR mirror plasma production if such an approach resulted in further optimization of the soft x-ray source characteristics.

An additional feature of possible importance to soft x-ray source selection is the maximum exposable wafer size while maintaining a prescribed limit on penumbral blur of the mask pattern image. A figure of merit can be defined for x-ray source candidates by combining the time-averaged x-ray emission intensity and the maximum exposable wafer area to determine an estimate of expected "wafer throughput" or wafer exposure rate as the total area of wafer exposed per unit time (e.g., cm^2/h). We now proceed to perform a simplified estimate of wafer exposure rates for the equilibrium ECR plasmas predicted by ECRIAXS.

Consider the geometry of Fig. 11. From one volume element $dV = r\,dr\,d\theta\,dz$ of plasma, it can be calculated that the x-ray power incident on the wafer is approximately:

$$P_{\rm inc} = \int dV \int d\Omega \left(\frac{d^2P}{dV\,d\Omega}\right)$$

$$= \int\int\int r\,dr\,d\theta\,dz\,\Omega_0(r,\theta,z)\left(\frac{1}{4\pi}\frac{dP}{dV}\right), \quad (24)$$

where dV is a plasma volume element, $d\Omega$ is the elemental solid angle into which the x rays from dV are emitted, $\Omega_0(r,\theta,z)$ is the solid angle subtended by the wafer (relative to the volume element dV "point source"), and it has been assumed that the x-ray emission is isotropic into 4π sr while the plasma is transparent to the x-ray photons. Furthermore, it is assumed that Ω_0 is approximately independent of both radius r and azimuthal angle θ over the plasma column's cross section. Then

$$P_{\rm inc} \approx \int_0^L (S\,dz)\Omega_0(z)\left(\frac{1}{4\pi}\frac{dP}{dV}\right), \quad (25)$$

where $\Omega_0(z)$ can be approximated as

$$\Omega_0(z) \approx dA/(r_0 + z)^2. \quad (26)$$

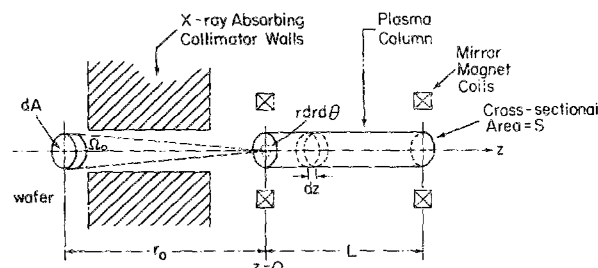

FIG. 11. Configuration for ECR mirror plasma as an x-ray source for x-ray lithography.

Putting Eq. (26) into Eq. (25) and integrating yields

$$P_{\rm inc} \approx \frac{dA}{4\pi}\left(\frac{dP}{dV}\right)\frac{SL}{r_0(r_0+L)}, \tag{27}$$

where dA is the area of the wafer, S is the cross-sectional area of the plasma column, L is the plasma length, r_0 is the wafer-to-plasma separation, and dP/dV is the x-ray power emitted by a unit volume of plasma into 4π Sr (e.g., W/cm^3).

We now proceed to calculate limits on plasma dimensions to avoid excessive penumbral blurring. The underlying principle is that in order to realize the opportunity for very fine pattern replication made possible by x-ray lithography, one must limit both plasma source and exposed wafer dimensions to avoid "penumbral blurring." This blurring of the lines produced on the wafer's photoresist is a consequence of the noninfinitesimal image size of the plasma source. For a long and thin plasma "cylinder," the penumbral blurring effects can be estimated by separately considering "on-axis" blurring, which depends on the plasma diameter [see Fig. 12 (a)], and "off-axis" blurring, which depends on the plasma column's length [see Fig. 12(b)].

In Figs. 12(a) and 12(b), the source diameter is $2r_p$ (where r_p is the plasma radius), the source length is L, and it is assumed that $2r_p \ll L$. In addition, g is the mask-to-resist distance (we assume proximity printing where $g \ll r_0$), Δ_1 is the on-axis penumbral blur, and we assume that the mask absorber thickness and the etching depth on the photoresist are infinitesimally small with respect to g and r_0. For these geometrical conditions we can estimate the on-axis resist pattern blur to be [cf. Fig. 12(a)]

$$\Delta_1 \approx g(2r_p/r_0), \tag{28}$$

based on simple trigonometric small-angle relationships. For comparative purposes, we use the design values of $g \approx 25$ μm and $\Delta_1 \leqslant 0.25$ μm taken from Ref. 33. This yields the design condition

$$2r_p/r_0 = \Delta_1/g \lesssim 0.01, \tag{29}$$

for acceptable amounts of on-axis blur. Thus, if we assume that $r_0 \approx 400$ cm, then we must choose $r_0 \approx 2$ cm.

Due to the considerable length of the plasma column, off-axis exposure of the resist can result in an effectively larger source size, as the exaggerated illustration in Fig. 12(b) suggests. Again, based on simple small-angle formulas one can estimate that the off-axis blur, Δ_2 is approximately

$$\Delta_2 \approx g\frac{L\tan\theta}{r_0} \approx g\frac{Lr_w}{r_0(r_0+L)}, \tag{30}$$

or, for a specified blur tolerance,

$$r_w \approx (\Delta_2/g)r_0(1+r_0/L) \tag{31}$$

gives the maximum wafer exposure radius. Again, using values of $\Delta_2 \leqslant 0.25$ μm, $g \approx 25$ μm, $r_0 \approx 400$ cm, and $L \approx 50$ cm, one obtains

$$r_w \approx 36 \text{ cm}. \tag{32}$$

Using the plasma and wafer dimensions obtained above,

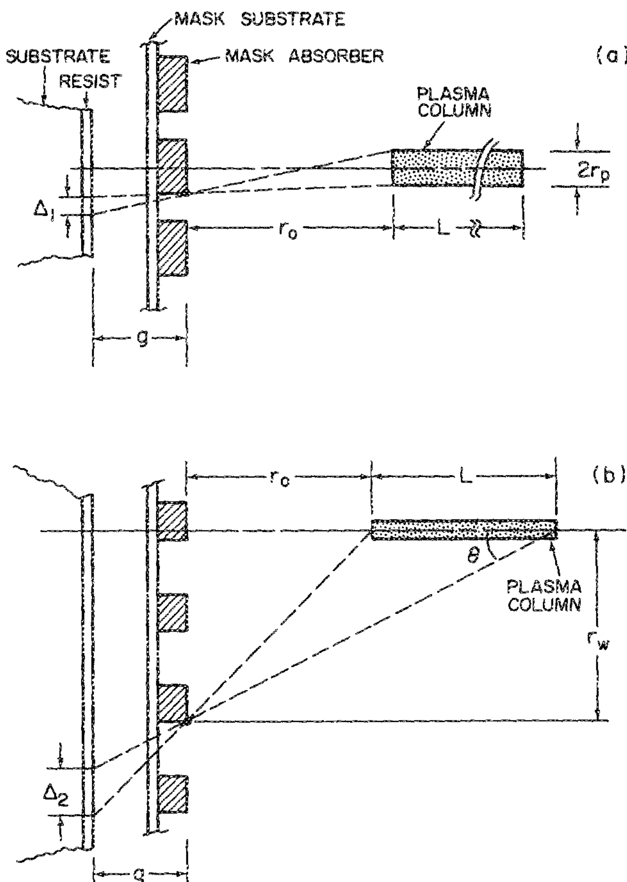

FIG. 12. Simplified schematic emphasizing the geometrical relationships which are pertinent to (a) on-axis and (b) off-axis penumbral blurring effects in an x-ray lithography device based on an ECR mirror plasma.

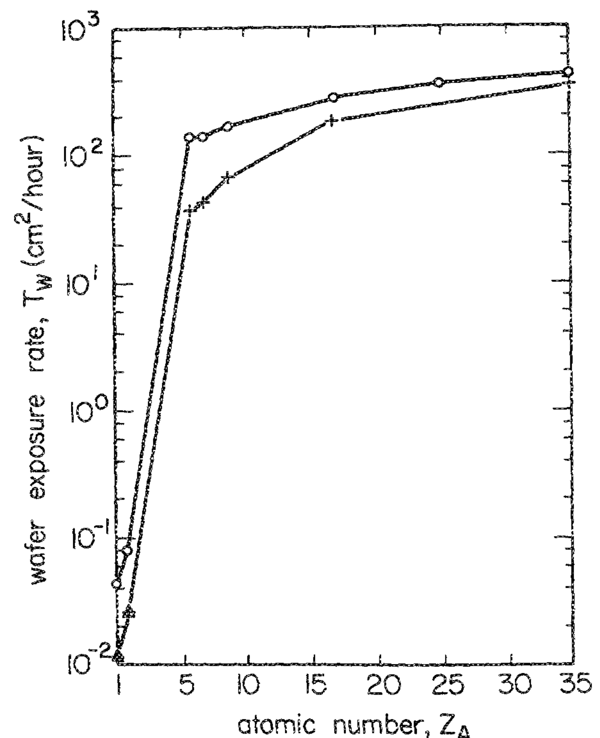

FIG. 13. Wafer exposure rate vs atomic number for two sets of plasma conditions: $n_e^h = 1.0\times10^{12}$ cm^{-3}, $T_e^h = 3.0$ keV, and $p_n = 1.0\times10^{-6}$ Torr (circles); $n_e^h = 5.0\times10^{11}$cm^{-3}, $T_e^h = 2.0$ keV, and $p_n = 2.0\times10^{-6}$ Torr (crosses).

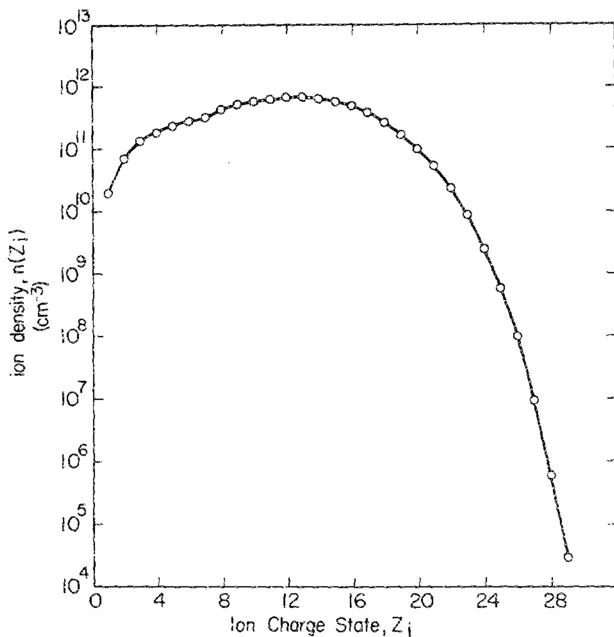

FIG. 14. Predicted CSD for an ECR krypton mirror plasma which has been optimized for x-ray lithography applications. Plasma parameters included: $n_e^h = 4.0\times 10^{12}$ cm^{-3}, $T_e^h = 10$ keV, $p_n = 7.0\times 10^{-6}$ Torr, $T_e^{th} = 10.0$ eV, $T_{ion} = 5.0$ eV, $n_e^{th} = 3.2\times 10^{13}$ cm^{-3}, and $\langle Z_{CSD}\rangle \approx 12.0$.

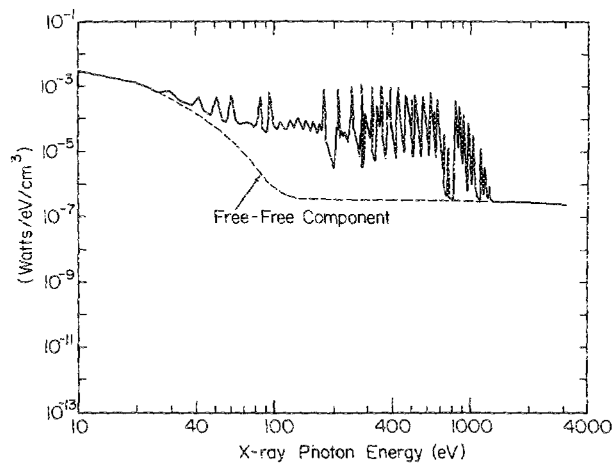

FIG. 15. X-ray power spectral density for the optimized krypton plasma of Fig. 14. The solid line represents the composite of line, bound-free, and free-free (bremsstrahlung) spectra; the dashed line indicates only the free-free component.

we substitute values into Eq. (27) to obtain

$$P_{inc} \approx (0.28\times 10^{-3})\, \frac{dP}{dV}\, dA \quad \text{W}, \tag{33}$$

where dP/dV is in W/cm^3 and dA is in cm^2.

From Ref. 34, we assume that photoresist exposure requires approximately 24 mJ/cm^2 of incident x-ray flux. Hence, to calculate the exposed wafer throughput (neglecting overhead time) we use

$$T_w\left(\frac{\text{cm}^3}{\text{h}}\right) \approx (1.5\times 10^5) P_{inc} \approx 75\left(\frac{dP}{dV}\right) dA.$$

Finally, the preceding specification on the maximum wafer radius $r_w \leqslant 36$ cm implies that this system can simultaneously expose a substantial wafer area without suffering excessive pattern blur. Hence, we finally obtain

$$T_w\left(\frac{\text{cm}^2}{\text{h}}\right) \approx (1.7\times 10^5)\, \frac{dP_{total}}{dV}\left(\frac{\text{W}}{\text{cm}^3}\right), \tag{34}$$

neglecting maintenance and overhead time. We note that for an alternative plasma discharge source,[33] $T_w \approx 120$ cm^2/h if we neglect overhead time.

Using Eq. (34) and the previously displayed results for x-ray emission power densities calculated by ECRIAXS, we have estimated the possible wafer exposure rates as a function of atomic number of the neutral gas species, hot electron distribution parameters, and neutral gas densities. Two representative cases are plotted in Fig. 13 as a function of atomic number Z_A. Generally, it appears that ECR mirror plasmas based on elements with $Z_A \gtrsim 7$ may be interesting candidates for soft x-ray sources with wafer exposure rates exceeding 100 W/cm^2. As seen from Eq. (34), the scaling of wafer exposure rates with hot electron parameters and neutral base pressure is identical to the dependence of x-ray power density on these factors. Thus, optimization of such wafer exposure rates is achieved by maximizing the x-ray emission power density (cf. Fig. 9).

To complete this study, we used ECRIAXS to compute an equilibrium krypton plasma which was "optimized" for maximum wafer exposure rate. The CSD for this somewhat optimistic case is displayed in Fig. 14 with the corresponding plasma conditions listed in the caption. The associated x-ray power density spectrum is shown in Fig. 15. The x-ray power density integrated over the 50 to 3000 eV band totaled

$$\frac{dP_{total}}{dV} \approx 0.111 \text{ W/cm}^3,$$

yielding an extremely attractive wafer exposure rate of $T_w \approx 1.9\times 10^4$ cm^2/h. For comparison, wafer exposure rates based on other soft x-ray sources have been estimated using arguments and approximations similar to those described above. These estimated rates are tabulated in Table I.

TABLE I. Comparison of wafer throughputs for various x-ray lithography sources.

Source	Wafer throughput (cm^2/h)
e-beam bombardment x-ray "tube"	3000[a]
laser-driven plasma	10^2–10^3[b]
plasma discharge	10^2–10^3[c]
synchrotron	2×10^3–10^4[d]
ECRIS	10^2–2×10^4[e]

[a] Based on discussion in Ref. 35.
[b] Based on Ref. 34; assumes a 4-cm^2 exposure area, 100 laser pulses per exposure band between 1 and 10 laser pulses per second.
[c] Based on Ref. 33; assumes a 4-cm^2 exposure area, and between 13 and 120 s per exposure.
[d] Based on Ref. 35; assumes that mask can handle radiation fluxes as high as 1 W/cm^2 and that wafer distortion limits simultaneous exposure area to less than 10 cm^2.
[e] Based on the modeling calculations in this paper.

VI. SUMMARY AND CONCLUSIONS

ECR mirror plasmas based on high Z atomic species involve complicated physical relationships between spatial particle transport and atomic processes. We have described a numerical code which represents a collection of simplified models for the purpose of calculating equilibrium ion charge state distributions and soft x-ray emission fluxes for such plasmas. Particular quantitative results were presented for a range of plasma parameters relevant to modest "laboratory-sized" devices.

For the cases considered, it was found that the highest average charge states and the highest soft x-ray outputs were predicted to be associated with the elements having the highest atomic numbers. In fact, it was found that the highest average charge states were associated with low neutral base pressures ($p_n \leqslant 5\times10^{-7}$ Torr), high hot electron densities ($n_e^h \geqslant 10^{12}$ cm^{-3}), and the modest ($T_e^h \approx 3$ keV) rather than high ($T_e^h \geqslant 10$ keV) hot electron temperatures. The highest soft x-ray outputs (in the 50 to 3000 eV band) were also associated with high hot electron densities and lower hot electron temperatures ($T_e^h \approx 3$ keV) but higher neutral pressures ($p_n \geqslant 2\times10^{-6}$ Torr). These latter observations on x-ray fluxes were correlated with those conditions which maximized the absolute values of ion densities in the lower charge states between $Z_i = 1$ and $Z_i \approx 5$. The most important reason for this relationship was the fact that x-ray fluxes were typically dominated by line emission from the lower energy transitions (approximately less than 500 eV) occurring within the lower charge state ions. There remains some question on whether the peak in soft x-ray output at lower values of T_e^h is an artificial consequence of having omitted inner shell fluorescent processes. This is a subject for future study with an improved model. Nevertheless, the implication of these results is that optimization of highly charged ion plasmas for different applications will require a capability to control and "tune" the hot electron fraction and temperature.

Finally, a very simplified model was described to estimate possible wafer exposure rates for an ECR mirror plasma used as an x-ray photolithography radiation source. The predicted wafer exposure rates of 100 to 20 000 cm^2/h compared very favorably with alternative soft x-ray sources. Admittedly, numerous approximations were made to obtain these exposure rate estimates. Nevertheless, the magnitude of the values calculated was promising and certainly warrants further study.

ACKNOWLEDGMENTS

The authors gratefully acknowledge generous assistance from Dr. H. I. West, Jr. of the Lawrence Livermore National Laboratory. Assistance from Dr. H. R. Griem, Dr. J. S. Wang, Dr. A. Sanchez, and Dr. E. Iglesias was also appreciated. This work was supported by the National Science Foundation. The computer stimulations were supported in part by the University of Maryland Computer Science Center.

[1]See, e.g., R. Geller, R. Jacquot, and M. Pontonnier, Rev. Sci. Instrum. **56**, 1050 (1985), and references contained therein.
[2]D. K. Smith and C. C. Petty, Bull. Am. Phys. Soc. **31**, 1511 (1986), paper 5P29.
[3]Y. Jongen and G. Ryckewaert, IEEE Trans. Nucl. Sci. **NS-30**, 2685 (1983).
[4]T. A. Antaya and Z. Q. Xie, in *Contributed Papers of the 7th Workshop on ECR Ion Sources*, Kernforschungsanlage Jülich, Jülich Report No. *Jül-Conf-57*, edited by Hans Beuscher (ISSN 0344-5798, Jülich, West Germany, 1986).
[5]F. Aldabe, J. H. Booske, R. F. Ellis, and W. D. Getty, Bull. Am. Phys. Soc. **31**, 1510 (1986), paper 5P28.
[6]D. J. Clark, J. G. Kalnins, and C. M. Lyneis, IEEE Trans. Nucl. Sci. **NS-30**, 2719 (1983).
[7]D. C. Gregory, F. W. Meyer, A. Müller, and P. Defrance, Phys. Rev. A **34**, 3657 (1986).
[8]J. H. Booske, W. D. Getty, R. M. Gilgenbach, T. P. Goodman, E. J. Pitcher, and R. A. Jong, IEEE Trans. Plasma Sci. **14**, 592 (1986).
[9]H. I. West, Jr., Lawrence Livermore National Laboratory Report No. UCRL-53391 (1982).
[10]R. W. P. McWhirter, in *Plasma Diagnostic Techniques*, edited by R. H. Huddleston and S. L. Leonard (Academic, New York, 1965), Chap. 5.
[11]T. D. Rognlien and T. A. Cutler, Nucl. Fusion **20**, 1003 (1980).
[12]D. E. Baldwin, Lawrence Livermore National Laboratory Report No. UCID-18802 (1980).
[13]V. P. Pastukhov, Nucl. Fusion **14**, 3 (1974).
[14]L. Spitzer, Jr., *Physics of Fully Ionized Gases* (Interscience, New York, 1956).
[15]A. Müller and E. Salzborn, Phys. Lett. A **62**, 391 (1977).
[16]V. P. Zhadanov, Sov. Phys. JETP **48**, 611 (1978).
[17]W. Lotz, Z. Phys. **216**, 241 (1968); **220**, 466 (1969).
[18]T. A. Carlson, C. W. Nestor, Jr., N. Wasserman, and J. D. McDowell, At. Data **2**, 63 (1970).
[19]D. E. Post, R. V. Jensen, C. B. Tarter, W. H. Grasberger, and W. A. Lokke, At. Data Nucl. Data Tables **20**, 397 (1977).
[20]D. K. Smith (private communications, 1986).
[21]D. C. Gregory, F. W. Meyer, A. Müller, and P. Defrance, Phys. Rev. A **34**, 3657 (1986).
[22]M. E. Mauel, Phys. Fluids **27**, 2899 (1984).
[23]T. R. Stratton, in *Plasma Diagnostic Techniques*, edited by R. H. Huddleston and S. L. Leonard (Academic, New York, 1965), Chap. 8.
[24]W. J. Karzas and R. Latter, Astrophys. J. Suppl. **VI**, 167 (1961).
[25]H. R. Griem, in *Handbook of Plasma Physics*, edited by M. N. Rosenbluth and R. Z. Sagdeev, Volume I: *Basic Plasma Physics I*, edited by A. A. Galeev and R. N. Sudan (North-Holland, New York, 1983).
[26]H. R. Griem, *Plasma Spectroscopy* (McGraw-Hill, New York 1964).
[27]M. J. Seaton, in *Atomic and Molecular Processes*, edited by D. R. Bates (Academic, New York, 1962), p. 374.
[28]R. L. Kelly and L. J. Palumbo, Naval Research Laboratory Report No. 7599 (1973).
[29]H. R. Griem, private communication (1988).
[30]V. L. Jacobs and B. F. Rozsnyai, Phys. Rev. A **34**, 216 (1986).
[31]D. L. Smatlak, Bull. Am. Phys. Soc. **31**, 1584 (1986), paper 8I5.
[32]B. H. Quon, R. A. Dandl, W. DiVergilio, G. E. Guest, L. L. Lao, N. H. Lazar, T. K. Samec, and R. F. Wuerker, Phys. Fluids **28**, 1503 (1985).
[33]I. Okada, Y. Saitoh, S. Itabashi, and H. Yoshihara, J. Vac. Sci. Technol. **B4**, 243 (1986).
[34]F. O'Neill, M. C. Gower, I. C. E. Turcu, and Y. Owandano, Appl. Opt. **25**, 465 (1986).
[35]A. R. Neureuther, in *Synchrotron Radiation Research*, edited by H. Winick and S. Doniach (Plenum, New York, 1979), Chap. 7.